

PAPER

High-performance asymmetric supercapacitor based hierarchical NiCo_2O_4 @ carbon nanofibers//Activated multichannel carbon nanofibers

To cite this article: Ahmed G El-Deen *et al* 2020 *Nanotechnology* **31** 365404

View the [article online](#) for updates and enhancements.





IOP | ebooks™

Bringing together innovative digital publishing with leading authors from the global scientific community.

Start exploring the collection—download the first chapter of every title for free.

High-performance asymmetric supercapacitor based hierarchical NiCo_2O_4 @ carbon nanofibers//Activated multichannel carbon nanofibers

Ahmed G El-Deen^{1,2} , M Hussein El-Shafei^{2,3} , Amr Hessein^{2,4}, Ahmed H Hassanin⁵, N M Shaalan^{6,7} and Ahmed Abd El-Moneim^{2,8,9}

¹ Renewable Energy Science and Engineering Department, Faculty of Postgraduate Studies for Advanced Sciences (PSAS), Beni-Suef University, Beni-Suef 62511, Egypt

² Materials Science and Engineering Department, Egypt-Japan University of Science and Technology, Alexandria 21934, Egypt

³ Production Engineering and Mechanical Design Department, Faculty of Engineering, Mansoura University, El-Mansoura 35516, Egypt

⁴ Department of Mathematical and Physical Engineering, Faculty of Engineering (Shoubra), Benha University, Cairo 11614, Egypt

⁵ Department of Textile Engineering, Alexandria University, Alexandria, Egypt

⁶ Department of Physics, College of Science, King Faisal University, Al-Hasa 31982, P.O. Box 400, Saudi Arabia

⁷ Physics Department, Faculty of Science, University of Assiut, Assiut 71516, Egypt

⁸ GrapheneCenter of Excellence for Energy and electronic Applications, Egypt-Japan University of Science and Technology, Alexandria 21934, Egypt

⁹ Institute of Basic and Applied Sciences, Egypt-Japan University of Science and Technology, New Borg El Arab, Alexandria 21934, Egypt

E-mail: ag.eldeen@psas.bsu.edu.eg, ahmed.abdelmoneim@ejust.edu.eg and m_hussein_issa@yahoo.com

Received 29 March 2020, revised 17 May 2020

Accepted for publication 29 May 2020

Published 24 June 2020



Abstract

Synthesis of rational nanostructure design of hybrid materials including uniformly growing, stable and highly porous structures have received a great deal of attention for many energy storage applications. In this study, the positive electrode of the uniform distribution of NiCo_2O_4 nanorods anchored on carbon nanofibers has been successfully prepared by *in-situ* growth under the hydrothermal process. Whereas, the activated multichannel carbon nanofibers (AMCNFs) have been fabricated via electrospinning followed by alkaline activation as the negative electrode. The crystal phase, morphological structure for the proposed electrode materials were characterized by x-ray diffraction (XRD), Raman spectroscopy, scanning electron microscopy (SEM), and transmission electron microscopy (TEM). Moreover, the electrochemical behaviors were investigated using cyclic voltammetry (CV), galvanostatic charge and discharge (GCD) and electrochemical impedance spectroscopy (EIS) measurements. Compared to the neat CNFs and the pristine NiCo_2O_4 , the NiCo_2O_4 @CNFs hybrid electrodes showed better electrochemical performance and achieved a high specific capacitance up to 649 F g^{-1} at a current density of 3 A g^{-1} . The optimized NiCo_2O_4 @CNFs//AMCNFs asymmetric device achieved a high energy density of 38.5 Wh kg^{-1} with a power density of 1.6 kW kg^{-1} and possessed excellent recyclability with 93.1% capacitance retention over 6000 charging/discharging cycles. Overall, the proposed study introduces a facile strategy for the robust design of hybrid structured as effective nanomaterials based electrode for high-performance electrochemical supercapacitors.

Keywords: hierarchical NiCo_2O_4 , carbon nanofibers, hybrid nanocomposite, asymmetric supercapacitors

(Some figures may appear in colour only in the online journal)

1. Introduction

The availability of affordable clean, safe, and sustainable energy poses one of the biggest challenges of the 21st century. The fast development of electronic devices and electric cars leads to the increasing energy demand [1,2]. Consequently, great efforts have been devoted to developing an effective, low-cost, and eco-friendly materials-based electrode for energy storage systems. Batteries and supercapacitors are considering as the most common and effective technologies for high electrochemical performance of conversion and storage systems [3–5]. Among all energy storage devices, supercapacitors have attracted a considerable interest in recent years due to their outstanding power density, long cycling lifetime, fast charging rates, and environmentally safe [6]. Currently, supercapacitors have been widely applied in LED flash sources, power backup, medical devices, and different portable electronics where they were introduced as a promising and scalable technique in the second generation of energy storage devices [1,7]. However, supercapacitors usually suffer from low energy density and fast discharge time compared to the rechargeable batteries [8].

Most of the commercial supercapacitors mainly used carbon-based electrode materials including carbon nanotubes [9], grapheme [10–12], carbon onion [13], carbon cloth [14], and carbon nanofibers which storage of the electrical energy based on electric double-layer capacitance (EDLC) effect [15,16]. Unfortunately, carbon-derived materials have low specific capacitances and low energy densities. The ideal supercapacitor device should deal with a large operating voltage and a higher energy density while keeping long cycling lifetime to meet the energy required for modern electrical devices [17–19]. In order to improve the energy density (E), both of specific capacitance (Cs) and cell potential (V) should be increased according to the following equation: $(E = 0.5 \text{ CV}^2)$ [20,21]. In the past few years, numerous extensive efforts have been dedicated to improve the performance of the asymmetric supercapacitors via combining nanostructured carbon based-materials that have high EDLCs with the pseudocapacitive nanomaterials such as metal oxide/hydroxide, conducting polymer, and carbon materials as composite electrode [22–24]. These pseudocapacitive materials, such as MnO_2 , RuO_2 , V_2O_5 , Fe_3O_4 , Fe_2O_3 , polyaniline, and polypyrrole those provide higher energy densities compared to EDLC of carbon material owing to their higher intrinsic specific capacitance and the operation at wide voltage range with maintaining excellent power density and cycling stability [25–31]. However and unfortunately, the conductive polymers have a low cycling stability, RuO_2 is too expensive, and most metal oxides and hydroxides have poor inherent electrical conductivity along with a very low specific surface area [32,33].

Among mono, bi and tri-metal oxides, NiCo_2O_4 , has attracted considerable attention as a good material based energy storage and sensor devices due to its unique intrinsic advantages including low-cost abundant elements, multiple oxide states, outstanding pseudocapacitive performance, and electrochemical efficiency [34–36]. Recently, great efforts have been done to enhance the capacitance of NiCo_2O_4 throughout the fabrication of different morphologies and nanostructures such as hollow spheres [37], nanosheets [38,39], nanowires [40,41], nanorods [42], and urchin-like structures in order to increase the exposed electrochemical surface area and also shorten the ion diffusion pathways [43,44]. Unfortunately, the improvements are still far away from the desired results because of the poor electron transfer rates and the low electrical conductivity [45]. Toward realizing applicable supercapacitor devices with high energy density and excellent electrochemical durability, the cell voltage window and the device specific capacitance should be remarkably improved. One of the ways for achieving this goal is combining of pseudocapacitive oxides as positive electrode materials with highly porous carbon electrode based negative electrodes in asymmetric supercapacitor device configurations [46,47].

Herein, a novel strategy is introduced to design and optimize robust asymmetric supercapacitor configuration. The proposed asymmetric design is consisting of an activated multichannel carbon nanofibers (AMCNFs) with ultrahigh surface area and excellent cycling stability that is employed as a negative electrode and the hierarchically porous NiCo_2O_4 nanorods anchored on CNFs (NiCo_2O_4 @CNFs) with a high surface area employed as the positive electrode. The NiCo_2O_4 @CNFs hybrid electrode was prepared by the facile and the cost-effective hydrothermal method which followed by calcination. Meanwhile, the AMCNFs were fabricated by the industrial applicable one-axial syringe electrospinning process and activation process. Our designed NiCo_2O_4 @CNFs//AMCNFs asymmetric supercapacitor can efficiently operate within a wide potential window of 1.6 V and can delivered a very good energy density of 38.5 Wh kg^{-1} at a power density of 1.6 kW kg^{-1} . In addition, a superior rate capability (24 Wh kg^{-1} at 4.8 kW kg^{-1}) as well as good cycle stability (93.12% capacitance retention after 6000 cycles) were also attained. This performance is among the highest values reported for supercapacitors operating with aqueous electrolytes.

2. Experimental

2.1. Materials

Polyacrylonitrile (PAN, $M_w \approx 150\,000 \text{ g.mol}^{-1}$) as precursor for CNF, cobalt (II) acetate tetrahydrate $[\text{Co}(\text{OAc})_2 \cdot 4\text{H}_2\text{O}]$, 98%, nickel (II) acetate tetrahydrate $[\text{Ni}(\text{OAc})_2 \cdot 4\text{H}_2\text{O}]$,

98%], urea [$\text{CO}(\text{NH}_2)_2$, >99%], and poly (methyl methacrylate) (PMMA, average $M_w = 120\,000\text{ g.mol}^{-1}$) were purchased from Sigma–Aldrich. N, N-Dimethylformamide (DMF), Ethanol, and allother chemical were obtained from Sigma–Aldrich as a reagent grad and used without further purifications.

2.2. Synthesis of ultrathin NiCo_2O_4 NR coated carbon nanofibers

The NiCo_2O_4 nanorods were synthesized using a hydrothermal method. Typically, 1 mmol of $\text{Co}(\text{OAc})_2 \cdot 4\text{H}_2\text{O}$ and 0.5 mmol of $\text{Ni}(\text{OAc})_2 \cdot 4\text{H}_2\text{O}$ with a molar ratio of 2:1 were dissolved in 75 ml doubled distilled water by stirring. After complete dissolving, 6 mmol of urea was then added to the solution and further stirred for another 0.5 hr. A 50 mg of the neat CNF was soaked into the obtained solution and sonicated for 1 hr. The mixture was transferred into a 100 ml Teflon lined stainless steel autoclave and maintained at $160\text{ }^\circ\text{C}$ for 16 hr. The autoclave was left to dry naturally to room temperature. The NiCo_2O_4 coated CNFs ($\text{NiCo}_2\text{O}_4@\text{CNFs}$) powder was collected and washed several times with ethanol and doubled distilled water to remove unreacted slats then dried overnight under vacuum at $60\text{ }^\circ\text{C}$. The dried $\text{NiCo}_2\text{O}_4@\text{CNFs}$ powder was calcinated under air at $380\text{ }^\circ\text{C}$ for 2 hr with a heating rate of $3\text{ }^\circ\text{C min}^{-1}$. The total wight of final product after calcination was 100 mg which corresponding to the coated NiCo_2O_4 onto surface of CNFs with ratio of (1:1). For more optimizations, four different ratios of $\text{NiCo}_2\text{O}_4@\text{CNFs}$ were prepared and tested, namely, $\text{NiCo}_2\text{O}_4@\text{CNFs}$ 1:4, $\text{NiCo}_2\text{O}_4@\text{CNFs}$ 1:2, $\text{NiCo}_2\text{O}_4@\text{CNFs}$ 1:1, and $\text{NiCo}_2\text{O}_4@\text{CNFs}$ 1.5:1, corresponding to 25, 50 100, and 150 wt% of NiCo_2O_4 loadings on the CNFs. Also, pristine ultrathin porous NiCo_2O_4 was fabricated using the same procedure in the absence of CNFs.

2.3. Preparation of activated multi-channel carbon nanofibers

The Multichannel carbon nanofibers were prepared according to our previous report [48]. Typically, 1 gm of PAN in 9 ml DMF and 0.7 gm of PMMA in 9.3 ml DMF were dissolved separately in two bottles with stirring in an oil bath at $75\text{ }^\circ\text{C}$ for 5 hr till complete dissolving and both solutions became clear. The two solutions then mixed together and transferred into one-axial syringe for electrospinning. A 23 kV potential difference was applied between the syringe needle and the ground collector, whereas the distance between them was adjusted to be 20 cm. The obtained electrospun polymeric nanofibers were dried at $70\text{ }^\circ\text{C}$ under vacuum overnight followed by a stabilization step at $280\text{ }^\circ\text{C}$ for 2 hr with a heating rate of $3\text{ }^\circ\text{C min}^{-1}$. The carbonization process was performed at $1000\text{ }^\circ\text{C}$ under an inert argon atmosphere in a tubular furnace for 5 hrs and with a $5\text{ }^\circ\text{C min}^{-1}$ heating rate. Finally, the fabricated multichannel carbon nanofibers (MCNFs) were activated by immersing into 6 M KOH under continuous stirring for 10 hr and dried overnight. Finally, the activated MCNFs (AMCNFs) were calcinated for 1 hr at $700\text{ }^\circ\text{C}$ under argon atmosphere

2.4. Materials characterization

The sample prepared at 100 wt% NiCo_2O_4 mass loading on the CNFs ($\text{NiCo}_2\text{O}_4@\text{CNFs}$ 1:1) is chosen as a representative for all $\text{NiCo}_2\text{O}_4@\text{CNFs}$ samples to conduct material characterization measurements. The surface morphology was studied by a JSM-5900 scanning electron microscope (SEM JEOL Ltd., Japan) and field-emission scanning electron microscope (FE-SEM Hitachi S-4700, Japan). The phase structure and crystallinity of the prepared electrode materials were analyzed using x-ray diffraction (XRD, PAN analytical Empyrean), with $\text{Cu K}\alpha$ ($\lambda = 1.540\text{ \AA}$) radiation and operated at 40 KV and 30 mA. High-resolution TEM images were obtained with Field emission transmission electron microscope (HRTEM, JEOL JEM-2010, Japan) operated at 200 kV. Raman spectroscopy was measured for the carbonized nanofibers CNF and $\text{NiCo}_2\text{O}_4@\text{CNF}$ nanocomposite using a Thermo Scientific DXR Raman microscope (Thermo Fisher Scientific Inc. MA, USA). The Brunauer-Emmett-Teller (BET) specific surface area of the prepared samples was characterized by N_2 adsorption-desorption isotherm using a micromeritics (ASAP 2010 V5.02H) analyzer.

2.5. Electrodes fabrication and electrochemical measurements

In order to fabricate the electrodes, the as-synthesized active materials were blended with acetylene black, and polyvinylidene fluoride (PVDF) in DMF with the exact ratio (85:10: 5). The prepared slurry was coated on a standard graphite foil as a current collector substrate then dried at $80\text{ }^\circ\text{C}$ under air. The dried electrodes were investigated using PARSTAT4000 + galvanostat/potentiostat and the data were acquired by the electrochemical workstation VersaStudio software. The electrochemical measurements including multistep cyclic voltammetry (CV) and galvanic charge/discharge test (GCD) were conducted in 1 M KOH solution within a potential window from -0.2 to 0.6 V using the symmetrical two-electrode system. The specific capacitance (C_s) of each active materials was calculated from GCD curves at different current densities using the following equation (1) [49,50],:

$$C_s = \frac{I \times \Delta t}{m \times \Delta V} \quad (1)$$

where I is the discharging current (A), Δt represents the discharging time in (s), ΔV is the voltage window (V) during the discharging process, and m is the total mass loading of the active electrode material (g).

Electrochemical impedance spectroscopy (EIS) measurements were also estimated under same conditions for all the formulations nanomaterials. The symmetrical cells are identical to the two-compartment cell mentioned above. The amplitude of the AC voltage was adjusted to 5 mV at 0 V bias DC voltage. The EIS data was recorded in the frequency range from 10 Hz to 100 kHz.

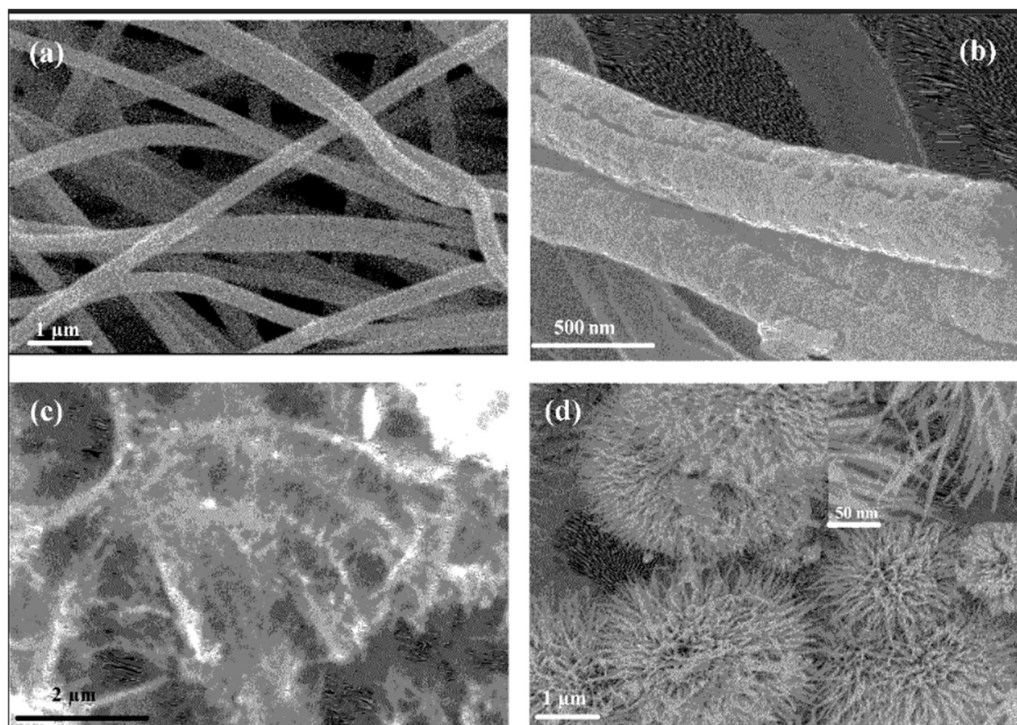


Figure 1. FE-SEM images for the pristine carbon nanofibers (a), activated multichannel carbon nanofibers (negative electrode) (b), NiCo₂O₄ NR anchored on carbon nanofibers (positive electrode) (c), and ultrathin NiCo₂O₄ nanorods (the inset image) is high magnification of nanorods (d).

2.6. Fabrications of the asymmetric supercapacitor device

To fabricate asymmetric supercapacitor (ASC) cell, the NiCo₂O₄@CNFs electrode and the AMCNFs electrode were assembled as the positive and the negative electrodes, respectively, which were separated by a cylindrical cellulose spacer. To achieve the highest possible capacitance value along with a wide operating voltage range from the ASC device, the ideal mass loading ratio of the both electrodes (m_+/m_-) was determined to be ~ 0.92 , using the charge-balance theory with the following equation (2) [29]:

$$\frac{m_+}{m_-} = \frac{C_- \times \Delta V_-}{C_+ \times \Delta V_+} \quad (2)$$

The total specific capacitance (C_t), energy density (E_t) and power density (P_t) of the ASC device were calculated using following Equations [51]:

$$C_t = \frac{I \times \Delta t}{m \times \Delta V} \text{ (F g}^{-1}\text{)} \quad (3)$$

$$E_t = \frac{C_t \Delta V^2}{7.2} \text{ (Wh Kg}^{-1}\text{)} \quad (4)$$

$$P_t = \frac{E_t \times 3600}{\Delta t} \text{ (W Kg}^{-1}\text{)} \quad (5)$$

where ΔV is the potential window, and Δt is the discharge time.

3. Results and discussion

3.1. Morphological shape and crystal structure

The electrospinning technique has been employed as a facile and low-cost fabrication method for the synthesis of a uniform nanofibers structure. The diameter and the porosity of the electrospun nanofibers can be controlled by the viscosity of the electrospinning polymer solution and the electrospinning parameters as well [52]. Herein, the carbon nanofibers (CNFs) were obtained by carbonization of Electrospun polyacrylonitrile (PAN) nanofibers at 1000 °C under an inert atmosphere. The CNFs showed a long and continuous nanofibrous morphology with an average diameter of 100 nm as revealed by the SEM micrograph in figure 1(a). It is worthy to mention that, the CNFs are free from any beads and cracks throughout its axial length which suggesting low charge transport resistance along their surface. On the other hand, the activated porous carbon nanofibers (AMCNFs) in figure 1(b) and as a result of surface alkaline activation by KOH, nanochannels and the nanopores have been induced on the surface of the neat CNFs surface.

The low-magnification SEM image in figure 1(c) of the NiCo₂O₄@CNFs declares a dense and uniform growth of NiCo₂O₄ hierarchical nanostructures on the CNFs surface. Obviously seen from the high-magnification SEM image in figure 1(d) that, the hierarchical NiCo₂O₄ nanostructures are highly porous and composed from ultrathin nanorods network with a very-sharp tip as clearly shown in the inset of figure 1(d). This open hierarchical structure of the

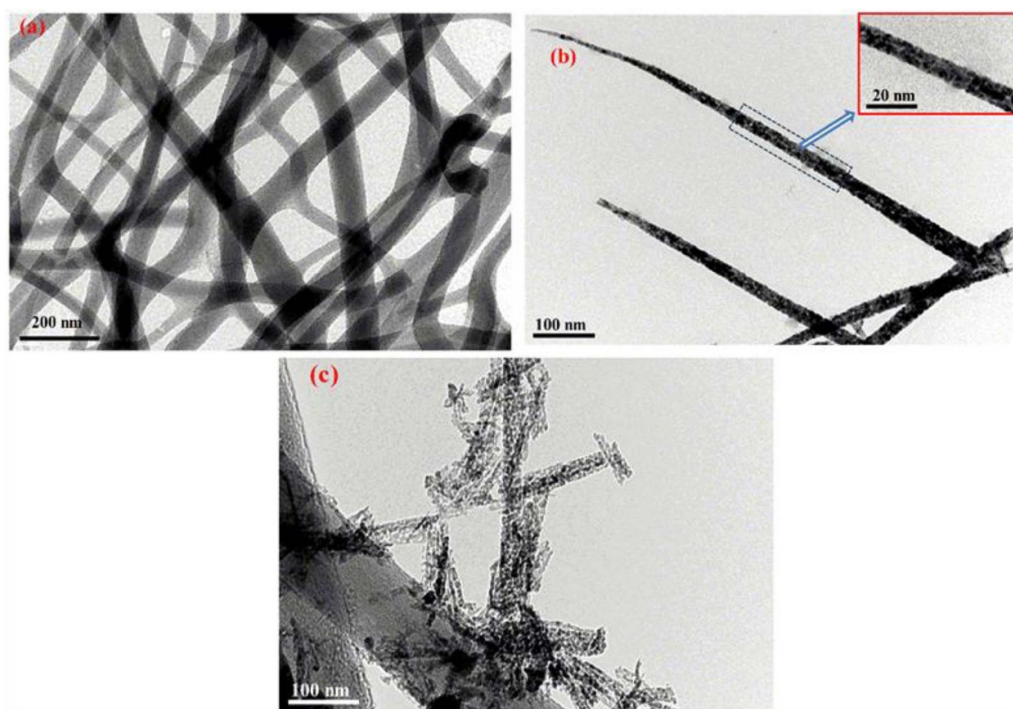
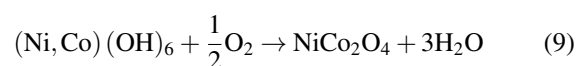
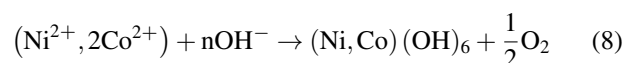
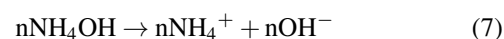


Figure 2. TEM images for carbon nanofibers (a), NiCo₂O₄ nanorods and the inset show high magnification of porous Nanorods (b) and NiCo₂O₄NR@CNFs (c).

NiCo₂O₄@CNFs offers a high surface area which is beneficial for electrolyte infiltration and provides also a plenty number of active sites.

The TEM image in figure 2(a) confirmed the continuous fiber structure of neat CNF without any beads or cracks throughout the axial length of the CNFs. The TEM image of individual NiCo₂O₄ nanorods in figure 2(b) clarifies the ultra-porous structure of the nanorods which composed of spinal bimetallic oxides with an average pores diameter of 2–4 nm which are connected and form the nanorods. Interestingly, the anchored porous NiCo₂O₄ nanorods are well-warped the CNFs as clearly appears in the TEM image presented in figure 2(c).

A growth mechanism of the NiCo₂O₄ hierarchical nanostructure can be proposed as follows: The dissociation of the metals nitrates in water is responsible for releasing Ni²⁺ and Co²⁺ metal cations. When the CNFs were added to the mixture, Ni²⁺ and Co²⁺ metal cations were electrostatically adsorbed on the surface of the CNFs. Meanwhile the hydrothermal process, the urea was decomposed with a controlled hydrolysis process producing a large number of OH⁻ ions during hydrothermal-decomposition reaction (6,7) [34]. During the extended hydrothermal treatment, mixed double hydroxides were possible to grow over the CNFs surface, reaction (8). Finally, the calcination of metal hydroxides-CNfs nanostructure at 360 °C for 2 hr releases the intercalated anions and the internally bonded water molecules and forming the spinel NiCo₂O₄, reaction (9). A summary of the spinel NiCo₂O₄ hierarchical nanostructure growth on the surface of the CNFs is schematically depicted in figure 3



The crystallographic phase purity of the NiCo₂O₄ nanorods is confirmed by powder XRD as shown in figure 4, where the six featured peaks of the cubic spinel phase were observed at 2θ values of 18.9, 31.2, 36.7, 44.6, 55.4, 59.1, and 65.0° can be assigned to (111), (220), (311), (222), (400), (511) and (440) planes of the highly pure spinel NiCo₂O₄ phase (JCPDS card No. 20-0781) [53]. No extra diffraction peaks belong to NiO or Co₃O₄ were noticed which ascertains the phase purity of the compound. The diffraction pattern of NiCo₂O₄@CNFs hybrid composite retains the typical diffraction peaks of NiCo₂O₄ superimposed on the broad characteristic (002) peak of the CNFs without a clear change in their angles position. This fact indicates that the load NiCo₂O₄ had good purity and incompletely covered the CNFs skeleton.

More insight into the structural evolution in the CNFs before and after loading with NiCo₂O₄ was conducted by performing the Raman spectroscopy and the acquired spectra are presented in figure 5. The spectrum of neat CNFs showed the two characteristic peaks of carbonaceous materials, namely the disorder D-band and the graphitic G-band at 1352 cm⁻¹ and 1585 cm⁻¹, respectively [54]. For NiCo₂O₄@CNFs nanocomposite, a new band is clearly visible in the low

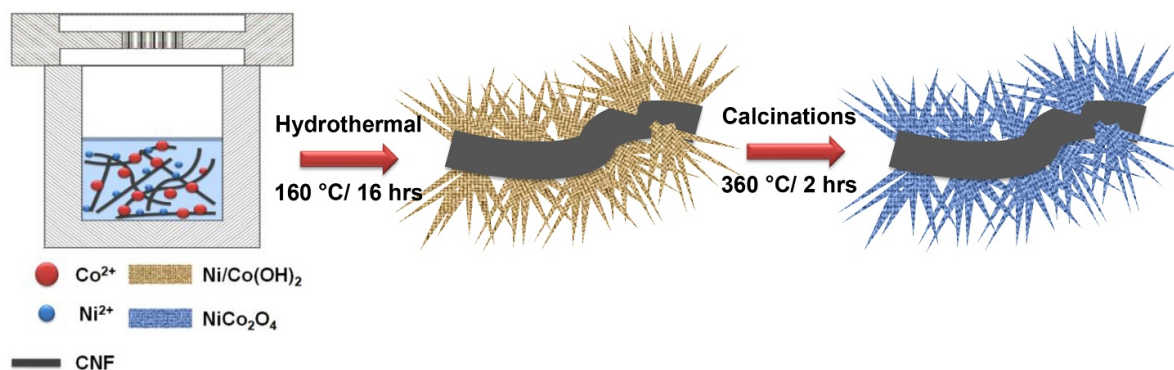


Figure 3. Schematic representation explains the proposed mechanism for porous NiCo₂O₄ nanorods formation on the surface of the CNFs.

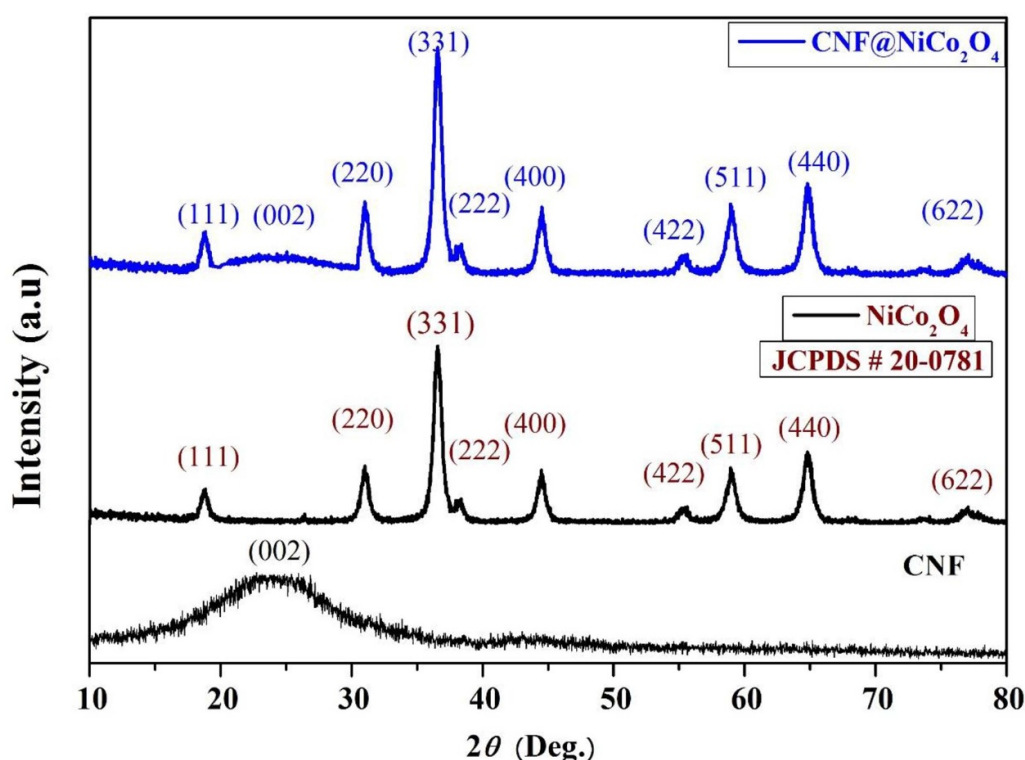


Figure 4. XRD pattern for neat CNFs, pristine NiCo₂O₄ nanorods, and NiCo₂O₄@CNFs hybrid nanocomposite.

wavenumber region at 658 cm⁻¹ associated with the A_{1g} Raman active modes of the NiCo₂O₄ spinel oxide [55]. The appearance of the NiCo₂O₄ band besides the D and G bands of the CNFs reflects the well-anchored NiCo₂O₄ hierarchical nanorods on the CNFs. There was no spectral feature related to NiO or Co₃O₄ detected in the Raman spectrum of the NiCo₂O₄@CNFs nanocomposite that is confirming the formation of a pure cubic spinel NiCo₂O₄ phase free of any secondary phases. The noticeable increase in the intensity of the G-band after loading with NiCo₂O₄ simultaneously with the decrease in the D-band intensity can be attributed to the enhancement in the graphitization of the CNFs by the action of hydrothermal treatment and the high temperature calcination process. As a result, the ratio (I_D/I_G) was decreased from 0.97 to be 0.78, suggesting a swifter charge transport and efficient charges collection mechanisms through the CNFs backbone.

The BET surface area and pore size distribution of the fabricated AMCNFs for the negative electrode application was investigated by N₂ adsorption/desorption isotherm as shown in figure 6(a). As shown in figure, the isotherm of the AMCNFs electrode revealed the characteristic (I-type) isotherm, indicating the presence of micro-pores as dominant pores inside AMCNFs and increasing of the slope adsorption isotherm and shape of desorption hysteresis confirming the presence of mesoporous as well [56,57]. The surface area of was calculated using the BET method for the fabricated AMCNFs which achieved high surface area (1357.13 m² g⁻¹) compared to reported neat CNFs (~60–250 m² g⁻¹) [58,59] or hollow CNFs (>200 m² g⁻¹) [60]. Moreover, the highly porous structure was estimated from BJH pore size distribution curve in figure 6(b), indicates that the AMCNFs have a dual pore geometry including mesoporous/microporous structure with an

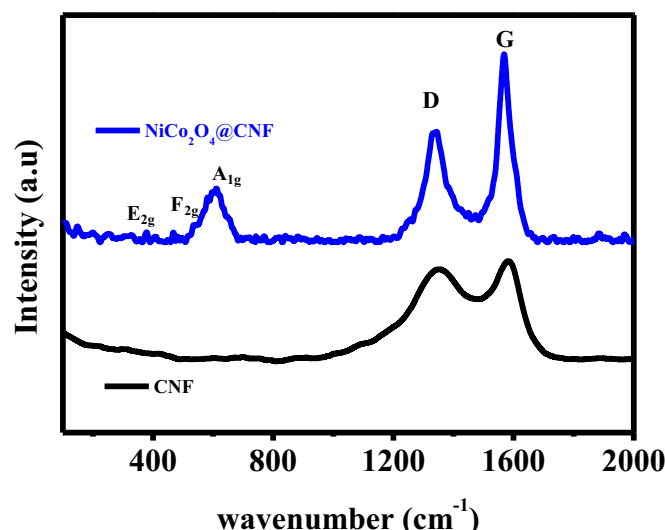


Figure 5. Raman spectra for neat CNFs and NiCo₂O₄ @CNFs hybrid nanocomposite.

average pore diameter of about 2.23 nm. Consequently, the high specific surface area and the extremely porous structure of AMCNFs have a significant impact on increasing the infiltration of the electrolyte ions at the electrode surface and also accelerate the ion diffusion pathway and thus a high capacitance and a fast charging rate could be achieved.

3.2. Electrochemical investigation of the electrodes

To estimate the electrochemical performances of the prepared materials, the electrochemical measurements: CV, GCD, and EIS measurements were performed on a two symmetric electrode configuration with 1 M KOH as the electrolyte solution. Figure 7(a) shows the typical CV curves of the NiCo₂O₄@CNFs symmetric device assembled from hybrid electrodes with different mass loading of the NiCo₂O₄ within a potential window ranging from −0.2 to 0.6 V at a scan rate of 10 mV s^{−1}. At the low NiCo₂O₄ mass loading of 25 wt% (NiCo₂O₄@CNFs 1:4), the CV voltammograms is nearly rectangular and symmetric. By increasing the NiCo₂O₄ loading, the CV curves start to take the ellipsoidal (semi-rectangular) shape indicating the relative increase in the contribution of the pseudocapacitive mechanism. Also, increasing the NiCo₂O₄ loading on the CNFs resulted in an increase the CV integral area until 100 wt% (NiCo₂O₄@CNFs 1:1) mass loading and then it decreased again. This implies that, the NiCo₂O₄@CNFs prepared at 100 wt% have the highest specific capacitance. The same trend was also obtained in the GCD curves in figure 7(b), such that the symmetric device fabricated based on the 100 wt% loading showed the highest charging and discharging times. The specific capacitances of all the NiCo₂O₄@CNFs symmetric devices were calculated from the discharge curve at 3 A g^{−1} current density according to equation (3), and the results are summarized in figure 7(c). The highest specific capacitance of 649 F g^{−1} was calculated to the symmetric NiCo₂O₄@CNFs (100 wt%) device that is over

performing the other fabricated devices measured at the same current density.

Figure 8(a) shows the cyclic voltammograms of the neat CNFs, the porous NiCo₂O₄ nanorods, and the hybrid NiCo₂O₄@CNFs of ratio 1:1 (100 wt%) electrodes at a scan rate of 10 mV s^{−1}. The CV curve of the hybrid NiCo₂O₄@CNF electrode demonstrates a larger integral area than that of NiCo₂O₄ or CNFs electrodes indicating higher specific capacitance. The Superiority of the NiCo₂O₄@CNFs electrode was originated from the anchoring of the hierarchical NiCo₂O₄ nanorods on CNFs' surface which plays the synergistic role in enhancing the electrolyte ions diffusion throughout the hybrid nanocomposite. Moreover, the improvement of interfacial specific surface area, the better electrical conductivity of CNFs that provides faster paths for charges collection, and additionally combining of the pseudocapacitive behaviour and electrical double layer capacitance were also responsible for the improved the energy storage and the capacitive behavior of the hybrid nanocomposite.

A comparison between the galvanic charge/discharge (GCD) profiles for the porous NiCo₂O₄, the neat CNFs, and the NiCo₂O₄@CNFs of ratio 1:1 (100 wt%) electrodes acquired at a current density of 3 A g^{−1} is shown in figure 8(b). Typically, the GCD profile of the pristine NiCo₂O₄ nanorods shows a lightly asymmetric shape than the CNFs. This indicates the quasi-reversible characteristic and nonlinear discharge profile due to the dominant of the Faradaic behaviour of the NiCo₂O₄ electrode. On the other hand, the GCD of the NiCo₂O₄@CNFs electrode attained a lower voltage drop (IR drop) compared to the pristine NiCo₂O₄ electrode and almost near to symmetric profile which due to the contribution of the EDLC effect from CNFs in the composite electrode. In general, the IR drop decreased and both charging and discharging times were much longer with the NiCo₂O₄ loading on CNFs' surface, in an agreement with the CV results.

Figure 8(c) shows the CV voltammograms of the NiCo₂O₄@CNFs (100 wt%) electrodes recorded at different sweep rates with a range of 10 to 50 mV s^{−1} to evaluate its dynamic capacitive behavior. The NiCo₂O₄@CNFs electrode showed a very small deviation in CV curves and unchanged semi-rectangular shape with increasing the scan rate which validates the high reversible Faradaic reactions, the good mass transport, and the excellent performance of the NiCo₂O₄@CNFs hybrid electrode.

Figure 8(d) displays the GCD curves for the hybrid NiCo₂O₄@CNFs (100 wt%) electrode at different current densities from 3 to 12 A g^{−1} to better understand its electrochemical performance. As can be seen, the charging and discharging times decreased with increasing the applied current density. Also, the symmetric GCD profile was conserved at all current densities with a tiny small IR drop. Thus, the admirable rate reversibility of the hybrid NiCo₂O₄@CNFs electrode and its noteworthy enhancement in the swift charge transfer rates can be inferred.

For the evaluation of the high-capacitive capability of the proposed hybrid electrode, the specific capacitances of the pristine NiCo₂O₄, the neat CNFs, and the NiCo₂O₄@CNFs (100 wt%) electrodes were calculated and

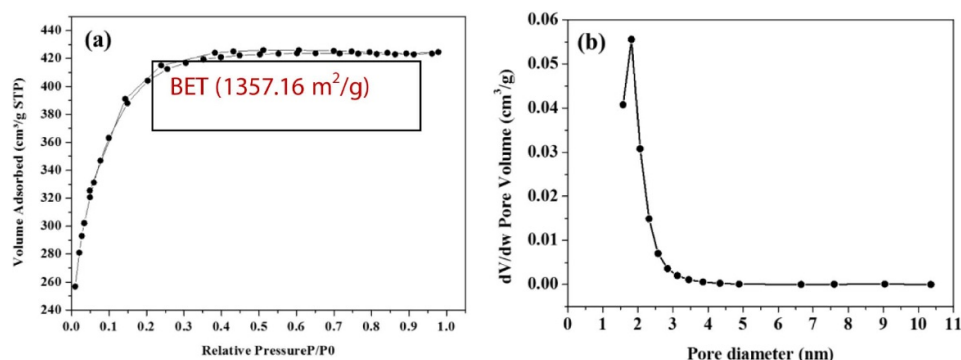


Figure 6. (a) N₂ adsorption/desorption isotherm, and (b) pore size distribution for the prepared the NiCo₂O₄@CNFs nanocomposite.

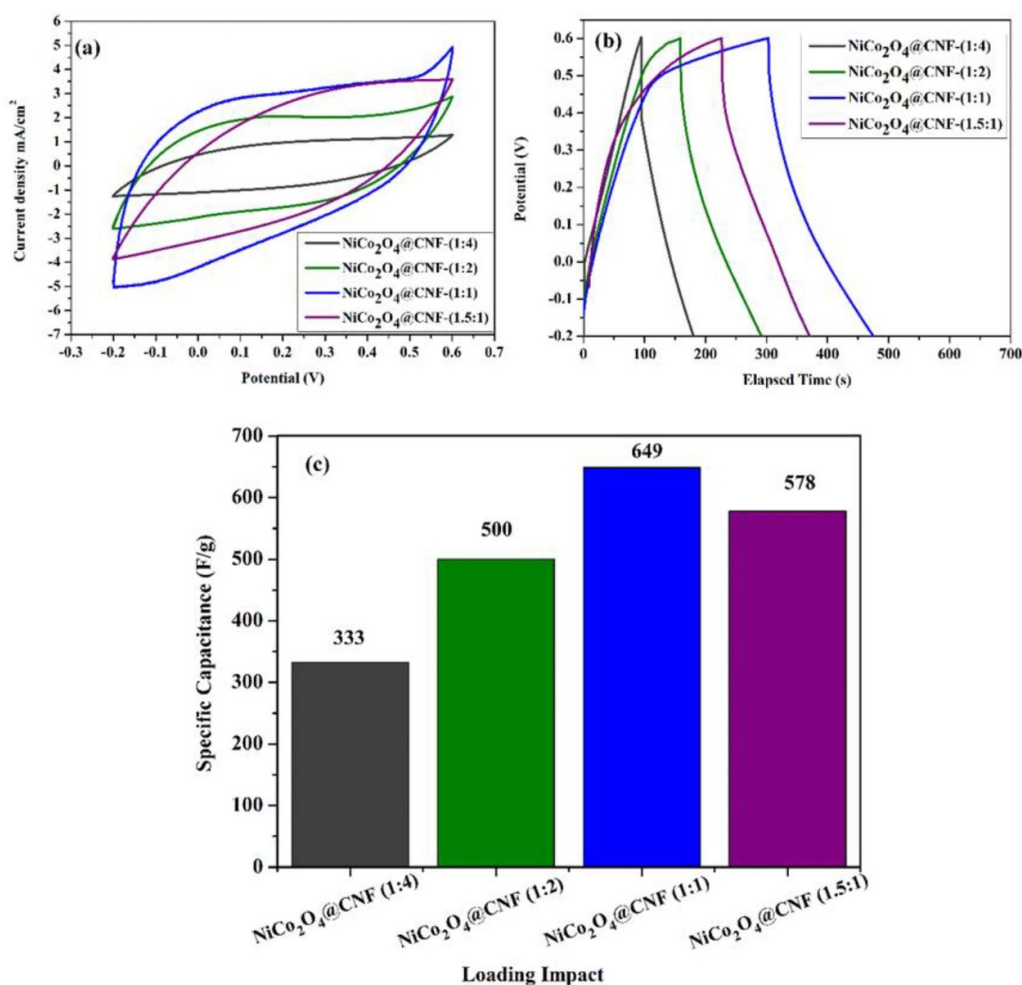


Figure 7. (a) Cyclic voltammetry of the prepared nanocomposite with different loading of NiCo₂O₄ at a scan rate of 10 mV s⁻¹ in aqueous 1.0 M KOH (b) Charge/discharge plot for various loading NiCo₂O₄ of into composite electrodes at a current density of 3 A g⁻¹, (c) specific capacitance versus loading impact of the fabricated materials at a current density of 3 A g⁻¹.

plotted in figure 8(e). The hybrid NiCo₂O₄@CNFs electrode achieved the highest superior specific capacitance of 649 F g⁻¹ compared to the pristine NiCo₂O₄ 260 F g⁻¹ and only 66 F g⁻¹ for the neat CNF at the same current density of 3 A g⁻¹. Furthermore, the hybrid NiCo₂O₄@CNFs electrode maintained the superior higher specific capacitance values overall

applied current densities. However, the decreases in capacitance observed with the increase of the charging-discharging current may be mainly attributed to the decrease in ions adsorption and diffusion rate capability from the electrolyte to the electrode at high charging-discharging rates [25–29]. This fact was not observed only in the hybrid electrode but

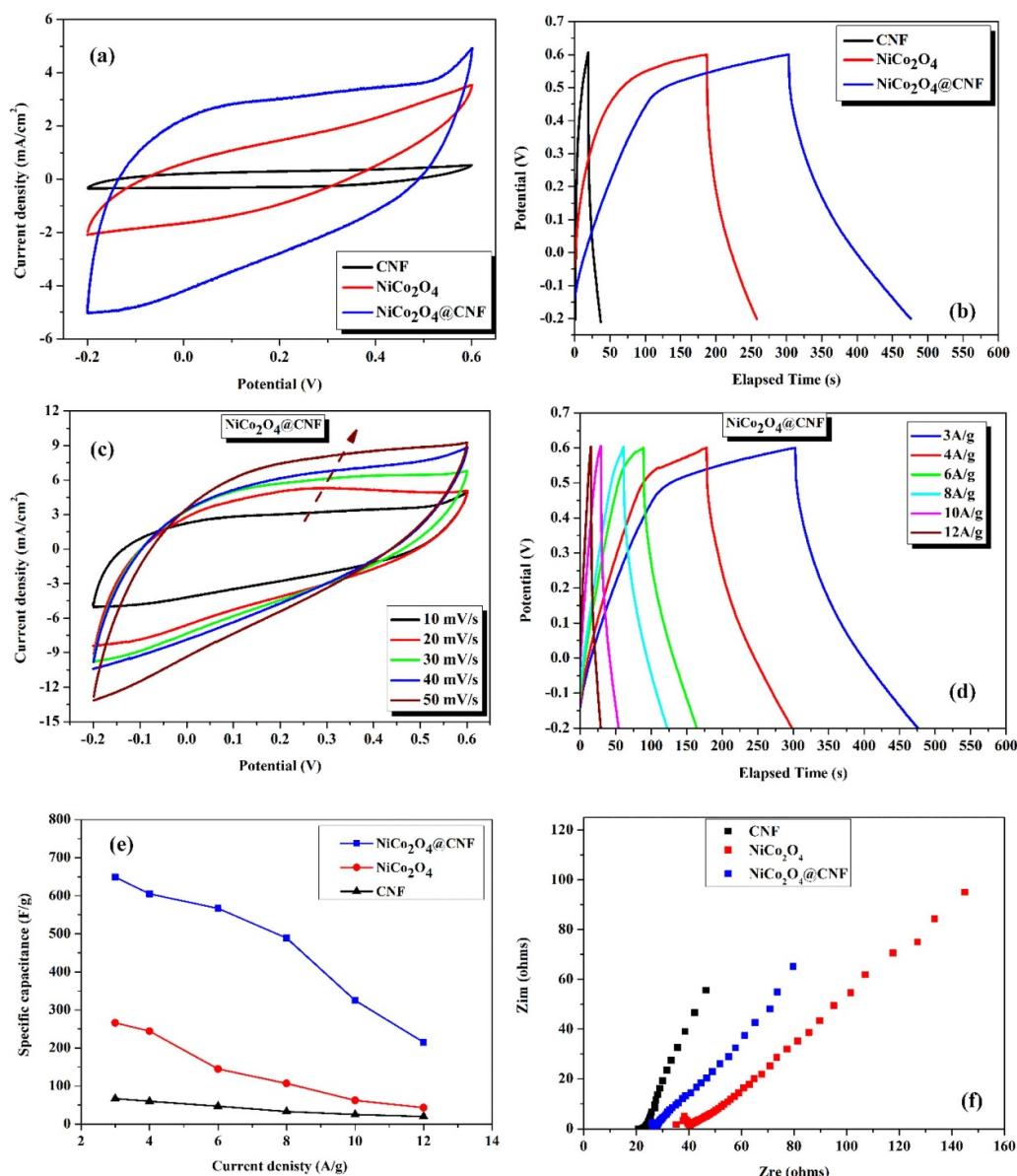


Figure 8. (a) Cyclic voltammetry of the fabricated electrode at a scan rate of 10 mV s⁻¹ in aqueous 1.0 M KOH electrolyte as symmetric two-electrode systems, (b) Charge/discharge plot for CNFs, NiCo₂O₄ and NiCo₂O₄@CNFs of ratio 1:1 (100 wt%) electrodes at a current density of 3 A g⁻¹, (c), (d) CV and chronopotentiometry curves of the NiCo₂O₄@CNFs composite electrode, (e) specific capacitance of the symmetric electrode materials as function of current density and (f) Electrochemical impedance spectra for the fabricated symmetric devices.

also observed for the other neat CNFs and porous NiCo₂O₄ electrodes.

The electrochemical impedance spectroscopy (EIS) is an efficient and useful measurement employed here to determine the internal resistances and changes of the interfacial electrochemical performance for the electrode materials. Figure 8(f) displays the EIS Nyquist plots of the NiCo₂O₄, the CNFs and the NiCo₂O₄@CNFs of ratio 1:1 (100 wt%) electrodes measured in the frequency range of 10 Hz to 100 kHz. In the case of the high-frequency region, the Nyquist plots have a small semicircle followed by a straight line in the low-frequency region which is a typical capacitor behavior. The intercept of the Nyquist plot with the real impedance axis at the

high-frequency is a measure of the equivalent series resistance (ESR). Meanwhile, the charge transfer resistance (R_{ct}) represented by the arc comes from both electric double layer effect and faradic reactions at the electrode surface. The increasing slope reflects the capacitive nature of the porous electrode [61]. The neat CNFs electrode showed the lowest ESR $\sim 20 \Omega$, reflecting its high intrinsic conductivity. The higher ESR of 36Ω obtained from the porous NiCo₂O₄ nanorods is due to the intrinsic conductivity of bimetallic oxide semiconductors [62]. The anchoring of NiCo₂O₄ on the highly-conductive CNFs scaffold in the hybrid electrode has led to improve the electrical conductivity of pristine NiCo₂O₄ and to the small ESR of about 23Ω achieved. These results confirmed the very

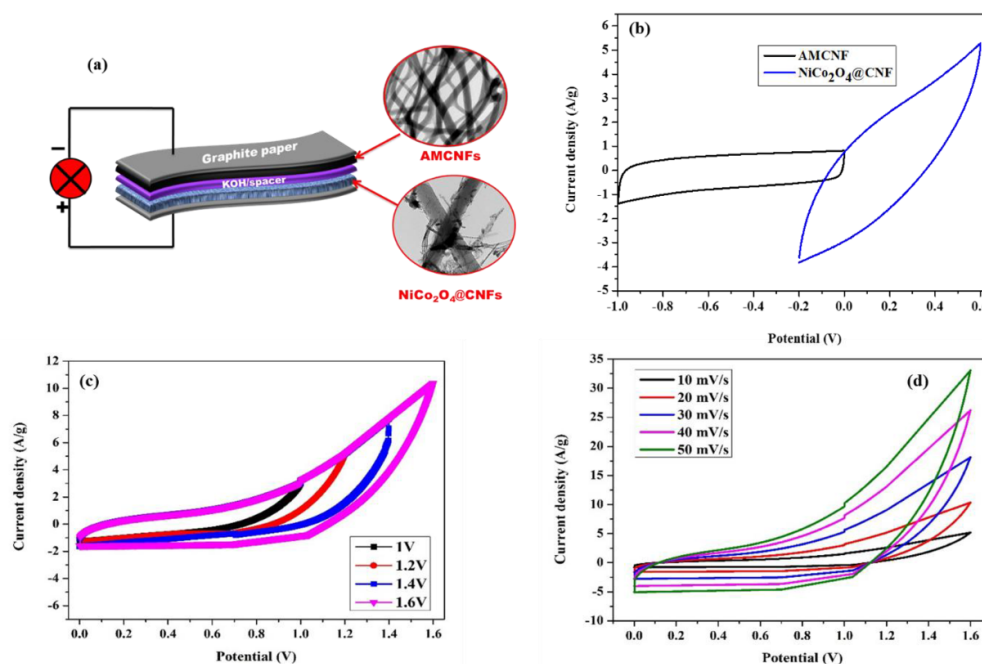


Figure 9. (a) Schematic diagram of the asymmetric $\text{NiCo}_2\text{O}_4\text{@CNFs//AMCNF}$ device Configuration, (b) Cyclic voltammetry of AMCNFs and $\text{NiCo}_2\text{O}_4\text{@CNFs}$ electrodes at a scan rate of 10 mV s^{-1} -based half-cell unite, (c) CV curves investigated at various potential windows at scan rate of 10 mV s^{-1} and (d) CV curves of the asymmetric device at different scan rates.

low ionic resistance of the electrolyte with small interfacial contact resistance between the surface of electrode materials and current collector.

In brief, this proposed hybrid $\text{NiCo}_2\text{O}_4\text{@CNFs}$ electrode attained significant improvements in both resistive and capacitive performances as a result of the NiCo_2O_4 deposition on the CNFs scaffold. The superior specific capacitance of the as-prepared $\text{NiCo}_2\text{O}_4\text{@CNFs}$ electrode can be attributed not only to the synergistic integration of EDLC and pseudocapacitance, but also to the highly-exposed active surface area, ultrathin and porous features, robust chemical stability, shorter ion pathways, and fast electron transport provided by the hierarchical nanostructure.

3.3. Electrochemical performance of the ($\text{NiCo}_2\text{O}_4\text{@CNFs//AMCNFs}$) ASC device

To realize the actual performance for a real SC devices, an asymmetric supercapacitor (ASC) device was assembled based on the $\text{NiCo}_2\text{O}_4\text{@CNFs}$ of ratio 1:1 (100 wt%) electrode as the anode (positive electrode) and the AMCNFs electrode as the cathode (negative electrode) with a 1.0 M KOH electrolyte as shown in the schematic diagram in figure 9(a). The CV voltammograms of the $\text{NiCo}_2\text{O}_4\text{@CNFs}$ and the AMCNFs electrodes at the different potential windows are presented in figure 9(b). This provides us with the validity and the applicability of the proposed asymmetric device configuration to deal with a voltage range of 1.6 V. Figure 9(c) displays the CV test of the $\text{NiCo}_2\text{O}_4\text{@CNFs//AMCNFs}$ ASC device performed at different potential windows from 1.0 to 1.6 V. Seeing that, the ASC device revealed a stable performance even at a wide

voltage window up to 1.6 V in the alkaline aqueous electrolyte. Interestingly, the incorporation of the CNFs with the NiCo_2O_4 in the $\text{NiCo}_2\text{O}_4\text{@CNFs}$ hybrid electrode lead to improve the operating potential from 1 to 1.6 V and the CV curves displayed a nearly rectangular shape of the typical capacitive behaviour.

Figure 9(d) shows the CV plots of the $\text{NiCo}_2\text{O}_4\text{@CNFs}$ ASC cell at a 1.6 V potential window measured at scan rates from 10 to 50 mV s^{-1} in 1.0 M KOH electrolyte. With increasing the scan rate, the enclosed area of the CV curves also increased while keeping quasi-rectangular shape. These obtained results refer to the good capacitive behaviour that is originating from the successful incorporation of the highly-conductive and chemically inert carbon nanofibers in both the positive and the negative electrodes of the ASC device. It worth mentioning that, the proposed ASC device provides a much higher operating potential of (1.6 V) compared to conventional activated carbon symmetric capacitors (0.8–1.0 V) under the same test conditions. This interesting behaviour is essentially attributed to the promising integration between the two charge storage mechanisms; the EDLC and the pseudocapacitance. Also, it can be ascribed to the combination of the $\text{NiCo}_2\text{O}_4\text{@CNFs}$ and the AMCNFs as the positive and the negative electrodes with a wide and high operating potential as well as the high specific capacitances.

The GCD tests of the fabricated $\text{NiCo}_2\text{O}_4\text{@CNFs//AMCNFs}$ ASC device were carried out at a constant current density of 2 A g^{-1} and for different charging potential windows ranging from 0.8 V to 1.6 V and demonstrated in figure 10(a). The assembled cell showed a linear relationship between the cell voltage and the discharging time. The obtained GCD profiles

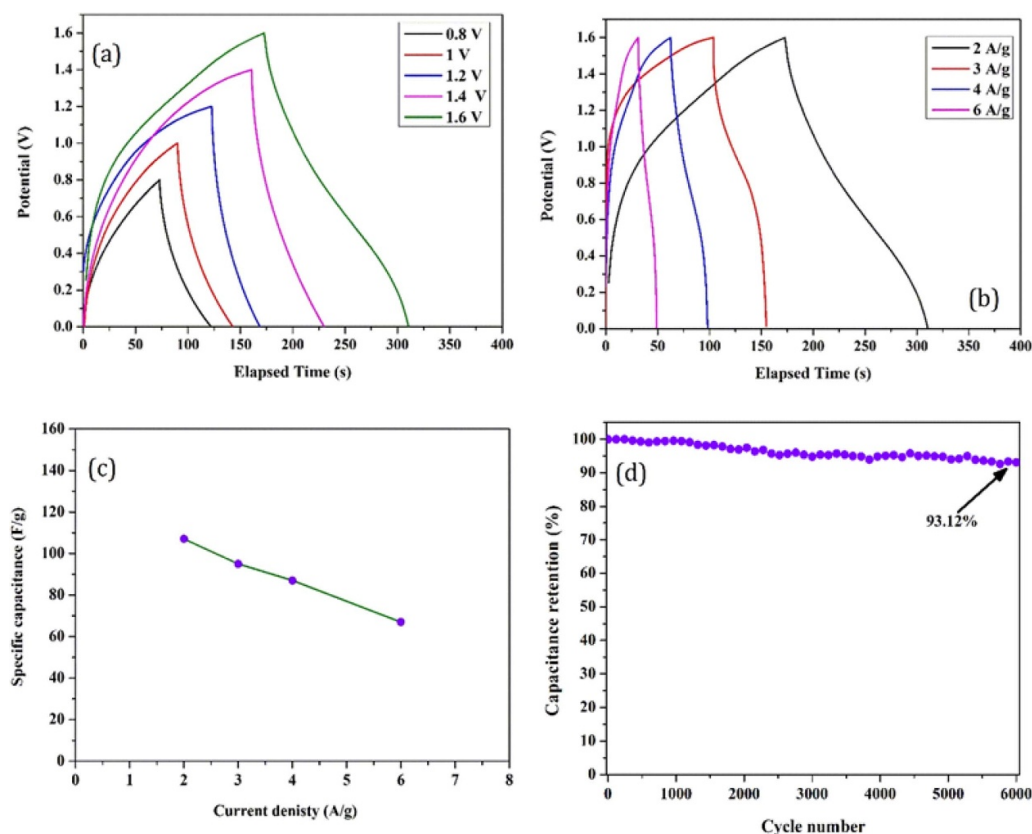


Figure 10. (a) Galvanostatic charge–discharge curves of the asymmetric $\text{NiCo}_2\text{O}_4@\text{CNFs}/\text{AMCNFs}$ device at different voltage windows under current density of 2 A g^{-1} , (b) charge–discharge curves at various current densities, (c) specific capacitances plot versus current densities, and (d) cycling stability test over 6000 cycles for the fabricated asymmetric device at current density of 6 A g^{-1} .

were also symmetrical in shapes and with only minimal IR drops demonstrating the superior capacitive property and the durable reversibility. Furthermore, no deviation in GCD curves was observed when they acquired at various current densities as declared in figure 10(b). The GCD curves almost retained the symmetric trend at all investigated current densities implying a high Coulombic efficiency of the fabricated device and also affirming its versatility of working under high operating voltages and currents.

The specific capacitances of the asymmetric $\text{NiCo}_2\text{O}_4@\text{CNFs}/\text{AMCNFs}$ device were calculated at different current densities and graphically summarized in figure 10(c). Specific capacitances of 107, 95, 87, and 67 F g^{-1} at current densities of 2, 3, 4, and 6 A g^{-1} , respectively, were estimated. The GCD cycling stability test performed at 6 A g^{-1} showed for 6000 cycle showed satisfying capacitance retention figure 10(d) such that, the ASC device maintains about 93.1% from its initial value by the end of the test.

Figure 11(a) depicts the Nyquist plot for the assembled $\text{NiCo}_2\text{O}_4@\text{CNFs}/\text{AMCNFs}$ ASC device before and after the stability test. Both EIS have similar behavior including small quasi-semicircle in the high-to-medium frequency region and a low-frequency linear part with approximately 45° declination angle. The two EIS spectra are well fitted to the equivalent circuit shown in the inset of figure 11(a). In the equivalent circuit, R_1 represents the ESR value, R_2 is the charge transfer resistance, W_2 is electrolyte diffusion (Warburg) impedance,

and C_2 is the double layer capacitance [34,63,64]. As shown, a small deviation in can be observed in high-frequency region after the stability test, which can be attributed to the polarization effect and the high specific current. However, the low equivalent series resistance (R_1) and the typical electrochemical behavior are sustained after the 6000-cycling stability.

For real capacitor devices, the energy density (E , Wh kg^{-1}) the power density (P , KW Kg^{-1}) are the most two important merits to evaluate the capacitive performance of supercapacitors. Herein, a maximum energy density of 38.5 Wh kg^{-1} at a power density of 1.6 kW kg^{-1} can be achieved by the assembled $\text{NiCo}_2\text{O}_4@\text{CNFs}/\text{AMCNFs}$ ASC device. Even at a high-power density of 4.8 kW kg^{-1} , an energy density 24 Wh kg^{-1} can be obtained. Although the energy densities were reduced with increasing the power densities, the energy density of the $\text{NiCo}_2\text{O}_4@\text{CNFs}/\text{AMCNFs}$ ASC cell at similar power densities is superior to those of the asymmetric supercapacitors reported on the NiCo_2O_4 or even on the NiCo_2S_4 nanostructured materials as presented in the Ragone plot in figure 11(b). For instance, our ASC configuration outweighs the reported asymmetric devices including $\text{NiCo}_2\text{O}_4\text{HS}/\text{AC}$ (11.6 Wh kg^{-1} at 5.22 kW kg^{-1}) [65], $\text{NiCo}_2\text{O}_4/\text{AC}$ (6.8 Wh kg^{-1} at 2.85 kW kg^{-1}) [66], $\text{NiCo}_2\text{S}_4@\text{Gr}/\text{AC}$ (19.9 Wh kg^{-1} at 6.8 k Wh kg^{-1}) [67], $\text{NiCo}_2\text{O}_4/\text{AC}$ (9.7 Wh kg^{-1} at 1.1 kW kg^{-1}) [68], and $\text{NiCo}_2\text{O}_4@\text{Gr}/\text{HFACs}$ (28 Wh kg^{-1} at 1.9 k W kg^{-1}) [69].

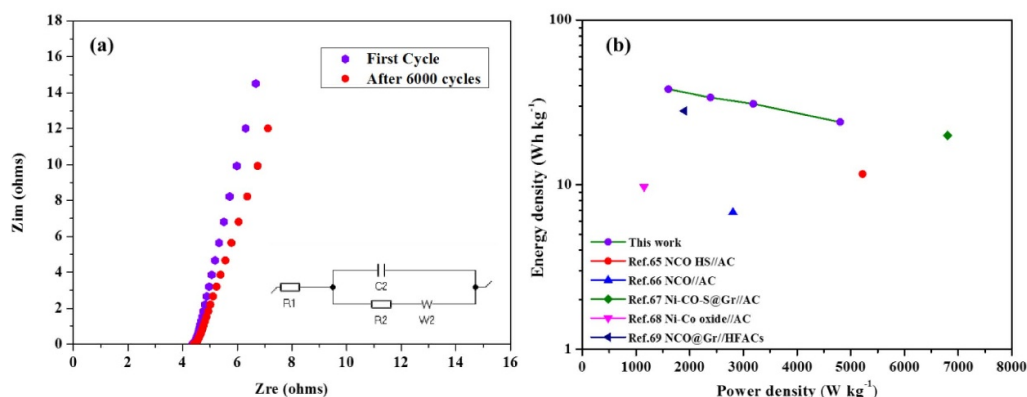


Figure 11. (a) Nyquist plot before and after 6000 cycles of the ASC device (the inset is equivalent circuit), (b) Ragone plot for the asymmetric NiCo_2O_4 @CNFs//AMCNFs device compared with recent reported values in the literatures.

4. Conclusions

We successfully fabricated highly-performance asymmetrical supercapacitor devices composed of the hybrid NiCo_2O_4 @CNFs electrode as the positive electrodes and AMCNFs electrode as the negative electrodes for practical supercapacitor applications. The NiCo_2O_4 @CNFs was synthesized via the facile and cost-effective hydrothermal method, whereas the AMCNFs was prepared by post-treatment surface activation of carbon nanofibers in alkaline media. The capacitance and the overall electrochemical performance of NiCo_2O_4 @CNFs are distinctly higher than the neat carbon nanofibers as well as the pristine NiCo_2O_4 . Typically, anchoring of porous hierarchical NiCo_2O_4 nanorods onto high electrically conductive and the chemically inert carbon nanofibers has a distinct impact on the electrochemical capacitance such as avoiding the limitations of electrical double layer capacitance of the CNFs through enhancing the ionic transport, increasing the interfacial surface area, and also pseudo-capacitance effect. Additionally, the use of AMCNFs as a negative electrode has a significant impact to increase the potential range and to decrease the equivalent series resistance. The asymmetric cell device assembled using NiCo_2O_4 @CNFs//AMCNFs demonstrated a maximum energy density (38.5 Wh kg^{-1}) at a power density (1.6 kW kg^{-1}), and at high power density (4.8 kW kg^{-1}) the energy density (24 Wh kg^{-1}) can also be achieved. Moreover, a remarkable recyclability was achieved, such that the developed ASC device maintained >93 % of its initial performance during 6000 charging/discharging cycles. The proposed asymmetric electrode material can pave the way for designing novel composite electrode materials for high-performance asymmetric supercapacitor devices.

Acknowledgments

The authors gratefully acknowledge the Missions Sector-Higher Education Ministry, Egypt, for the financial support for this work, and the Materials Science and Engineering Department at E-JUST. This study was also

supported by Grants (ID 31306) and Reintegration Grant (ID 33340) supported by science and technology development fund (STDF) in Egypt.

Author contributions

Ahmed Abd El Moneim directed the study. Ahmed G El-Deen and M Hussein El-Shafei proposed the idea and the procedure for the experimental design and did the experiments. Ahmed G El-Deen, Amr Hessein, and M Hussein El-Shafei were responsible for the data analysis. Ahmed G El-Deen, Amr Hessein, M Hussein El-Shafei, Ahmed H Hassanin, N M Shaalan and Ahmed Abd El Moneim discussed the results and contributed to writing the manuscript.

ORCID iDs

Ahmed G El-Deen  <https://orcid.org/0000-0001-7042-9126>

M Hussein El-Shafei  <https://orcid.org/0000-0003-2253-8840>

References

- [1] Yoo H D, Markevich E, Salitra G, Sharon D and Aurbach D 2014 On the challenge of developing advanced technologies for electrochemical energy storage and conversion *Mater. Today* **17** 110–21
- [2] Armaroli N and Balzani V 2007 The future of energy supply: challenges and opportunities *Angew. Chem. Int. Ed. Engl.* **46** 52–66
- [3] Conway B E 1999 *Electrochemical Supercapacitors: Scientific Fundamentals and Technological Applications* (New York: Plenum Publishers)
- [4] Simon P, Gogotsi Y and Dunn B 2014 Where do batteries end and supercapacitors begin? *Science* **343** 1210–1
- [5] Isacfranklin M, Ravi G, Yuvakkumar R, Kumar P, Velauthapillai D, Saravanakumar B, Thambidurai M and Dang C 2020 Urchin like NiCo_2O_4 /rGO nanocomposite for high energy asymmetric storage applications *Ceram. Int.*
- [6] Liu C, Li F, Ma L P and Cheng H M 2010 Advanced materials for energy storage *Adv. Mater.* **22** E28–E62

- [7] Mosa I M, Pattammattel A, Kadimisetty K, Pande P, El-Kady M F, Bishop G W, Novak M, Kaner R B, Basu A K and Kumar C V 2017 Ultrathin graphene–protein supercapacitors for miniaturized bioelectronics *Adv. Energy Mater.*
- [8] Zhang J, Jiang J, Li H and Zhao X 2011 A high-performance asymmetric supercapacitor fabricated with graphene-based electrodes *Energy Environ. Sci.* **4** 4009–15
- [9] Futaba D N, Hata K, Yamada T, Hiraoka T, Hayamizu Y, Kakudate Y, Tanaike O, Hatori H, Yumura M and Iijima S 2006 Shape-engineerable and highly densely packed single-walled carbon nanotubes and their application as super-capacitor electrodes *Nat. Mater.* **5** 987–94
- [10] Zhang L L, Zhou R and Zhao X 2010 Graphene-based materials as supercapacitor electrodes *J. Mater. Chem.* **20** 5983–92
- [11] Ghoniem E, Mori S and Abdel-Moniem A 2016 Low-cost flexible supercapacitors based on laser reduced graphene oxide supported on polyethylene terephthalate substrate *J. Power Sources* **324** 272–81
- [12] Gamil M, Nageh H, Bkrey I, Sayed S, El-Bab A M F, Nakamura K, Tabata O and El-Moneim A A 2014 Graphene-based strain gauge on a flexible substrate *Sensors Mater.* **26** 699–709
- [13] Portet C, Yushin G and Gogotsi Y 2007 Electrochemical performance of carbon onions, nanodiamonds, carbon black and multiwalled nanotubes in electrical double layer capacitors *Carbon* **45** 2511–8
- [14] Schmitt C, Pröbstle H and Fricke J 2001 Carbon cloth-reinforced and activated aerogel films for supercapacitors *J. Non-Cryst. Solids* **285** 277–82
- [15] Barranco V, Lillo-Rodenas M, Linares-Solano A, Oya A, Pico F, Ibanez J, Agullo-Rueda F, Amarilla J and Rojo J 2010 Amorphous carbon nanofibers and their activated carbon nanofibers as supercapacitor electrodes *J. Phys. Chem. C* **114** 10302–7
- [16] El-Shafei M H, Hassanin A H, Shaalan N, Sharshar T and El-Moneim A 2020 Free-standing interconnected carbon nanofiber electrodes: new structural designs for supercapacitor application *Nanotechnology* **31** 185403
- [17] Dubal D, Ayyad O, Ruiz V and Gomez-Romero P 2015 Hybrid energy storage: the merging of battery and supercapacitor chemistries *Chem. Soc. Rev.* **44** 1777–90
- [18] Wang G, Zhang L and Zhang J 2012 A review of electrode materials for electrochemical supercapacitors *Chem. Soc. Rev.* **41** 797–828
- [19] Chabi S, Peng C, Hu D and Zhu Y 2014 Ideal three-dimensional electrode structures for electrochemical energy storage *Adv. Mater.* **26** 2440–5
- [20] Simon P and Gogotsi Y 2012 Capacitive energy storage in nanostructured carbon–electrolyte systems *Acc. Chem. Res.* **46** 1094–103
- [21] Sun S, Wang S, Li S, Li Y, Zhang Y, Chen J, Zhang Z, Fang S and Wang P 2016 Asymmetric supercapacitors based on a NiCo 2 O 4/three dimensional graphene composite and three dimensional graphene with high energy density *J. Mater. Chem. A* **4** 18646–53
- [22] He Y, Chen W, Li X, Zhang Z, Fu J, Zhao C and Xie E 2012 Freestanding three-dimensional graphene/MnO₂ composite networks as ultralight and flexible supercapacitor electrodes *ACS Nano* **7** 174–82
- [23] Zhang K, Zhang L L, Zhao X and Wu J 2010 Graphene/polyaniline nanofiber composites as supercapacitor electrodes *Chem. Mater.* **22** 1392–401
- [24] Mao L, Guan C, Huang X, Ke Q, Zhang Y and Wang J 2016 3D graphene-nickel hydroxide hydrogel electrode for high-performance supercapacitor *Electrochim. Acta* **196** 653–60
- [25] Wang Y, Guo J, Wang T, Shao J, Wang D and Yang Y-W 2015 Mesoporous transition metal oxides for supercapacitors *Nanomaterials* **5** 1667–89
- [26] Xu D, Xu Q, Wang K, Chen J and Chen Z 2013 Fabrication of free-standing hierarchical carbon nanofiber/graphene oxide/polyaniline films for supercapacitors *ACS Appl. Mater. Interfaces* **6** 200–9
- [27] Hassan S, Suzuki M, Mori S and El-Moneim A A 2014 MnO₂/carbon nanowall electrode for future energy storage application: effect of carbon nanowall growth period and MnO₂ mass loading *RSC Adv.* **4** 20479–88
- [28] El-Moneim A 2011 Mn–Mo–W-oxide anodes for oxygen evolution during seawater electrolysis for hydrogen production: effect of repeated anodic deposition *Int. J. Hydrog. Energy* **36** 13398–406
- [29] Ghaly H A, El-Deen A G, Souaya E R and Allam N K 2019 Asymmetric supercapacitors based on 3D graphene-wrapped V₂O₅ nanospheres and Fe₃O₄@ 3D graphene electrodes with high power and energy densities *Electrochim. Acta* **310** 58–69
- [30] Eskusson J, Rauwel P, Nerut J and Jänes A 2016 A hybrid capacitor based on Fe₃O₄-graphene nanocomposite/few-layer graphene in different aqueous electrolytes *J. Electrochem. Soc.* **163** A2768–A75
- [31] Kim G, Kang J, Choe G and Yim S 2017 Enhanced energy density of supercapacitors using hybrid electrodes based on Fe₂O₃ and MnO₂ nanoparticles *Int. J. Electrochem. Sci.* **12** 10015–22
- [32] Zhu Y, Wu Z, Jing M, Hou H, Yang Y, Zhang Y, Yang X, Song W, Jia X and Ji X 2015 Porous NiCo 2 O 4 spheres tuned through carbon quantum dots utilised as advanced materials for an asymmetric supercapacitor *J. Mater. Chem. A* **3** 866–77
- [33] Snook G A, Kao P and Best A S 2011 Conducting-polymer-based supercapacitor devices and electrodes *J. Power Sources* **196** 1–12
- [34] Padmanathan N and Selladurai S 2014 Controlled growth of spinel NiCo 2 O 4 nanostructures on carbon cloth as a superior electrode for supercapacitors *RSC Adv.* **4** 8341–9
- [35] Zhang Y, Wang J, Ye J, Wan P, Wei H, Zhao S, Li T and Hussain S 2016 NiCo₂O₄ arrays nanostructures on nickel foam: morphology control and application for pseudocapacitors *Ceram. Int.* **42** 14976–83
- [36] Zhang J, Chu R, Chen Y, Jiang H, Zeng Y, Zhang Y, Huang N M and Guo H 2019 Binder-free C@ NiCo₂O₄ on Ni foam with ultra-stable pseudocapacitive lithium ion storage *Nanotechnology* **30** 125402
- [37] Shen L, Yu L, Yu X Y, Zhang X and Lou X W D 2015 Self-templated formation of uniform NiCo₂O₄ hollow spheres with complex interior structures for lithium-ion batteries and supercapacitors *Angew. Chem. Int. Ed.* **54** 1868–72
- [38] Yuan C, Li J, Hou L, Zhang X, Shen L and Lou X W D 2012 Ultrathin mesoporous NiCo₂O₄ nanosheets supported on Ni foam as advanced electrodes for supercapacitors *Adv. Funct. Mater.* **22** 4592–7
- [39] Ren -Q-Q, Wang Z-B, Ke K, Zhang S-W and Yin B-S 2017 NiCo₂O₄ nanosheets and nanocones as additive-free anodes for high-performance Li-ion batteries *Ceram. Int.* **43** 13710–6
- [40] Huang L, Chen D, Ding Y, Feng S, Wang Z L and Liu M 2013 Nickel–cobalt hydroxide nanosheets coated on NiCo₂O₄ nanowires grown on carbon fiber paper for high-performance pseudocapacitors *Nano Lett.* **13** 3135–9
- [41] Zhang F, Ma J and Yao H 2019 Ultrathin Ni-MOF nanosheet coated NiCo₂O₄ nanowire arrays as a high-performance binder-free electrode for flexible hybrid supercapacitors *Ceram. Int.* **45** 24279–87

- [42] Zhang W, Xin W, Hu T, Gong Q, Gao T and Zhou G 2019 One-step synthesis of NiCo₂O₄ nanorods and firework-shaped microspheres formed with necklace-like structure for supercapacitor materials *Ceram. Int.* **45** 8406–13
- [43] Zhang G and Lou X W D 2013 Controlled growth of NiCo₂O₄ nanorods and ultrathin nanosheets on carbon nanofibers for high-performance supercapacitors *Sci. Rep.* **3** 1470
- [44] Zhang J, Chu R, Chen Y, Jiang H, Zhang Y, Huang N M and Guo H 2018 Electrodeposited binder-free NiCo₂O₄@ carbon nanofiber as a high performance anode for lithium ion batteries *Nanotechnology* **29** 125401
- [45] Kong D, Ren W, Cheng C, Wang Y, Huang Z and Yang H Y 2015 Three-dimensional NiCo₂O₄@ polypyrrole coaxial nanowire arrays on carbon textiles for high-performance flexible asymmetric solid-state supercapacitor *ACS Appl. Mater. Interfaces* **7** 21334–46
- [46] Feng L, Li G, Zhang S and Zhang Y X 2017 Decoration of carbon cloth by manganese oxides for flexible asymmetric supercapacitors *Ceram. Int.* **43** 8321–8
- [47] Cherusseri J, Kumar K S, Choudhary N, Nagaiah N, Jung Y, Roy T and Thomas J 2019 Novel mesoporous electrode materials for symmetric, asymmetric and hybrid supercapacitors *Nanotechnology* **30** 202001
- [48] El-Deen A G, Barakat N A, Khalil K A and Kim H Y 2013 Development of multi-channel carbon nanofibers as effective electrosorptive electrodes for a capacitive deionization process *J. Mater. Chem. A* **1** 11001–10
- [49] Barakat N A, El-Deen A G, Shin G, Park M and Kim H Y 2013 Novel Cd-doped Co/C nanoparticles for electrochemical supercapacitors *Mater. Lett.* **168**–71
- [50] Ma Y, Yu Z, Liu M, Song C, Huang X, Moliere M, Song G and Liao H 2019 Deposition of binder-free oxygen-vacancies NiCo₂O₄ based films with hollow microspheres via solution precursor thermal spray for supercapacitors *Ceram. Int.* **45** 10722–32
- [51] Zhang Y, Liu X, Wang S, Dou S and Li L 2016 Interconnected honeycomb-like porous carbon derived from plane tree fluff for high performance supercapacitors *J. Mater. Chem. A* **4** 10869–77
- [52] Huang Z-M, Zhang Y-Z, Kotaki M and Ramakrishna S 2003 A review on polymer nanofibers by electrospinning and their applications in nanocomposites *Compos. Sci. Technol.* **63** 2223–53
- [53] Khalid S, Cao C, Wang L and Zhu Y 2016 Microwave assisted synthesis of porous NiCo₂O₄ microspheres: application as high performance asymmetric and symmetric supercapacitors with large areal capacitance *Sci. Rep.* **6** 22699
- [54] Li W, Zhang L-S, Wang Q, Yu Y, Chen Z, Cao C-Y and Song W-G 2012 Low-cost synthesis of graphitic carbon nanofibers as excellent room temperature sensors for explosive gases *J. Mater. Chem.* **22** 15342–7
- [55] Al-Rubaye S, Rajagopalan R, Dou S X and Cheng Z 2017 Facile synthesis of a reduced graphene oxide wrapped porous NiCo₂O₄ composite with superior performance as an electrode material for supercapacitors *J. Mater. Chem. A* **5** 18989–97
- [56] Lee H-M, Kang H-R, An K-H, Kim H-G and Kim B-J 2013 Comparative studies of porous carbon nanofibers by various activation methods *Carbon Lett.* **14** 180–5
- [57] Wang G, Pan C, Wang L, Dong Q, Yu C, Zhao Z and Qiu J 2012 Activated carbon nanofiber webs made by electrospinning for capacitive deionization *Electrochim. Acta* **69** 65–70
- [58] Daraghme A, Hussain S, Saadeddin I, Servera L, Xuriguera E, Cornet A and Cirera A 2017 A study of carbon nanofibers and active carbon as symmetric supercapacitor in aqueous electrolyte: a comparative study *Nanoscale Res. Lett.* **12** 639
- [59] Zhi M, Liu S, Hong Z and Wu N 2014 Electrospun activated carbon nanofibers for supercapacitor electrodes *RSC Adv.* **4** 43619–23
- [60] El-Deen A G, Barakat N A, Khalil K A and Kim H Y 2014 Hollow carbon nanofibers as an effective electrode for brackish water desalination using the capacitive deionization process *New J. Chem.* **38** 198–205
- [61] Zhang D, Wen X, Shi L, Yan T and Zhang J 2012 Enhanced capacitive deionization of graphene/mesoporous carbon composites *Nanoscale* **4** 5440–6
- [62] Xia H, Wang Y, Lin J and Lu L 2012 Hydrothermal synthesis of MnO₂/CNT nanocomposite with a CNT core/porous MnO₂ sheath hierarchy architecture for supercapacitors *Nanoscale Res. Lett.* **7** 1–10
- [63] Liu F, Wang X, Hao J, Han S, Lian J and Jiang Q 2017 High density arrayed Ni/NiO core-shell nanospheres evenly distributed on graphene for ultrahigh performance supercapacitor *Sci. Rep.* **7** 1–10
- [64] Li D, Gong Y, Zhang Y, Luo C, Li W, Fu Q and Pan C 2015 Facile synthesis of carbon nanosphere/NiCo₂O₄ core-shell sub-microspheres for high performance supercapacitor *Sci. Rep.* **5** 1–8
- [65] Li X, Jiang L, Zhou C, Liu J and Zeng H 2015 Integrating large specific surface area and high conductivity in hydrogenated NiCo₂O₄ double-shell hollow spheres to improve supercapacitors *NPG Asia Mater.* **7** e165
- [66] Ding R, Qi L, Jia M and Wang H 2013 Facile and large-scale chemical synthesis of highly porous secondary submicron/micron-sized NiCo₂O₄ materials for high-performance aqueous hybrid AC-NiCo₂O₄ electrochemical capacitors *Electrochim. Acta* **107** 494–502
- [67] Yang J, Yu C, Fan X, Liang S, Li S, Huang H, Ling Z, Hao C and Qiu J 2016 Electroactive edge site-enriched nickel–cobalt sulfide into graphene frameworks for high-performance asymmetric supercapacitors *Energy Environ. Sci.* **9** 1299–307
- [68] Tang C, Tang Z and Gong H 2012 Hierarchically porous Ni-Co oxide for high reversibility asymmetric full-cell supercapacitors *J. Electrochem. Soc.* **159** A651–A6
- [69] Li Z, Xu Z, Wang H, Ding J, Zahiri B, Holt C M B, Tan X and Mitlin D 2014 Colossal pseudocapacitance in a high functionality–high surface area carbon anode doubles the energy of an asymmetric supercapacitor *Energy Environ. Sci.* **7** 1708–18